An intelligent poly aptamer-encoded DNA nanoclew for tumor site activated mitochondria-targeted photodynamic therapy and MR imaging

Minghui Chen [a,c,1], Hanbo Xu [a,d,1], Pengzhao Chang [a,1], Xueqi Li [a,c], Shuang Liu [b], Lingyue Xu [a], Kai Xu [a,c,**], Guohui Cheng [b,c,*]

[a] School of Medical Imaging, Xuzhou Medical University, Xuzhou, 221004, PR China
[b] School of Pharmacy, Xuzhou Medical University, Xuzhou, 221004, PR China
[c] Department of Radiology, Affiliated Hospital of Xuzhou Medical University, Xuzhou, 221006, PR China
[d] Department of Radiology, The Affiliated Lianyungang Hospital of Xuzhou Medical University, Lianyungang, 222000, PR China

ARTICLE INFO

ABSTRACT

Mitochondria-targeted photodynamic therapy (PDT) has emerged as one of the most promising antitumor therapies, as it significantly enhances the efficacy of photosensitizers. An efficient and biocompatible nanocarrier to deliver cationic photosensitizers (PSs) is vital for mitochondria-targeted PDT but still challenging. Herein, a poly-AS1411 aptamer DNA nanoclew (AS-AMD) synthesized via rolling circle amplification (RCA) is developed, incorporating mitochondria-targeted PSs (APNO) and paramagnetic Mn^{2+} for mitochondria-targeted PDT and magnetic resonance imaging (MRI). The AS1411 aptamer of AS-AMD has been engineered to enhance tumor targeting and cellular internalization. Paramagnetic Mn^{2+} released in the acidic tumor microenvironment promotes MRI performance of the tumor tissue and guides subsequent PDT. The released cationic APNO selectively targets the mitochondrial membrane and generates reactive oxygen species (ROS) that induce the apoptosis of 4T1 breast tumor cells. Additionally, AS-AMD exhibits effective tumor targeting in the 4T1-tumor-bearing mice model, significantly enhanced MRI performance and PDT efficacy. Therefore, this study introduces an interesting strategy to achieve efficient mitochondrial-targeted delivery of cationic PSs and provides a versatile biocompatible DNA nanoplatform for the development of nanotheranostic agents.

1. Introduction

Photodynamic therapy (PDT) is advantageous due to its non-invasiveness, minimal adverse effects, and non-resistant outcome, rendering it extraordinarily promising for the treatment of various cancers and has consequently garnered research attention [1–3]. The PDT relies on photosensitizers (PSs) exposed to specific laser wavelengths to generate cytotoxic reactive oxygen species (ROS), leading to the effective elimination of cancer cells. Due to the very brief lifetime (10–320 ns) and narrow diffusion radius (10–55 nm) of ROS, photodynamic cytotoxicity is largely dependent on the organelle localization of PSs within cells [2,4,5]. Because mitochondria are essential organelles for cell respiration and convergence sites for numerous lethal signal transduction pathways, mitochondria-targeted PDT tends to be more effective [6]. At present, many cationic nanocarriers decorated with triphenylphosphine and pyridinium have been developed to deliver PSs to mitochondria [7]. Although positively charged nanocarriers can promote mitochondrial adsorption, they also usually result in faster immune clearance and serious system toxicity [8,9]. Therefore, there is an urgent need for the on-demand design of efficient and biocompatible nanocarriers for mitochondria-targeted PDT.

Due to their inherent biocompatibility, programmable molecular recognition and structural controllability, self-assembled DNA nanostructures have received widespread attention in areas such as imaging, and drug delivery [10–14]. The highly programmable character of Watson-Crick base pairing enables researchers to assemble virtually any desired shape by programming DNA or RNA such as DNA Nanotubes, DNA bricks, DNA tetrahedrons, and DNA nanoparticles [15–19]. In addition, high drug-loading efficiency and effective intracellularization further endow DNA nanocarriers with promising potential in the field of

---

drug delivery [20–22]. The rational design of DNA nanostructures for the delivery of PSs can surmount the challenges associated with PDT [23,24]. However, to advance the application of DNA nanostructures for the delivery of PSs in mitochondria-targeted PDT, it is critical to enhancing its intelligent identification of tumor tissues and address the inherent stability of DNA.

The aptamer AS1411, with its guanine base abundance, selectively targets and adheres to nucleolin, a protein that is predominantly found on the surface of cancer cells. This trait has led to its prevalent application as a targeting ligand for the intelligent identification of tumor tissues for targeted antitumor treatments [25]. Nevertheless, monovalent functional nucleic acid constructs, such as the As1411 DNA monomer, have been studied previously, showing limited stability and affinity in biological settings [26]. Polynucleotide DNA (polyDNA) is an ultralong single-stranded DNA with multivalent functional sequences that offers improved stability in biological environments [27]. Therefore, poly-AS1411 aptamer-encoded DNA nanostructures would address the inherent stability of DNA nanostructures and provide more tumor-targeting probes, enhancing the intelligent and sensitive identification of tumor tissue to targeted antitumor treatments.

Herein, we reported a poly-AS1411 aptamer-encoded DNA nanoclew loaded cationic PSs for mitochondria-targeted PDT and MRI. AS1411 aptamer as multiple repeats was encoded in the circle template to obtain nanoclew of uniform size by Mn^{2+}-mediated rolling circle amplification (RCA) reaction. Then the synthesized mitochondria-targeted PSs APNO was embedded into the DNA interior by π-π stacking and electrostatic incorporation to obtain multifunctional DNA nanoclew (AS-AMD) (Fig. 1). AS1411 aptamer-encoded AS-AMD was engineered to enhance tumor targeting and cellular internalization. Paramagnetic Mn^{2+} released in the acidic tumor microenvironment enhance the MRI contrast of tumor, facilitating visualization and guiding the implementation of subsequent PDT. The released cationic APNO would be localized to the mitochondrial membrane to achieve mitochondria-targeted PDT under light irradiation. Hence, this investigation not only delineates a facile approach towards the fabrication of poly aptamer-encoded DNA nanoclew carriers with enhanced stability but

also proffers a promising tactic to augment the efficacy of PDT.

2. Experimental section

2.1. Materials and reagents

All pertinent materials and reagents have been meticulously documented in the supplementary information. The synthesized oligonucleotide sequences are laid out in Table S1.

2.2. Circularization of linear DNA

The phosphorylated strand DNA template was first formulated as 10 μM in 1 × PBS and heated at 90 °C for 5 min. Then, the TssDNA was cooled down by 0.5 °C every 30 s to 25 °C. Afterthat, the 10 pmol DNA template, 100 U ssDNA/RNA CircLigase and 1 × CircLigase buffer were fully mixed in 15 μL DEPC water. The mixture was incubated at 65 °C for 60 min. Then the mixtures were heated at 85 °C for 10 min and placed at ambient temperature for 10 min to obtain the cyclized DNA template (CT).

2.3. Preparation of AS-AMD

The reaction buffer contained 25 μL 10 × isothermal amplification buffer, 5 μL CT solution, 12.5 μL DNA primer solution (20 μM), 5 μL dNTP (10 mM), 47.6 μL 50 mM $MnCl_2$ solution, and 154.9 μL DEPC water. The reaction solution was placed in a PCR instrument and reacted at 95 °C for 5 min. After the mixture was cooled to ambient temperature, 6.5 μL Bst 2.0 DNA polymerase (8 U/μL) was added and reacted at 60 °C for 17 h. Afterthat, the reaction solution was maintained at 80 °C for 20 min to inactivate the polymerase to terminate the reaction. After the reaction mixture was centrifuged at 4000 rpm for 1.5 min, the lower precipitate was retained and stirred with APNO solution for 1 h at room temperature and then centrifuged to obtain APNO-loaded AS-AMD. Then the mixture was centrifuged at 4000 rpm for 1.5 min. The lower precipitate was placed in an ultrafiltration centrifuge tube (30 KD),
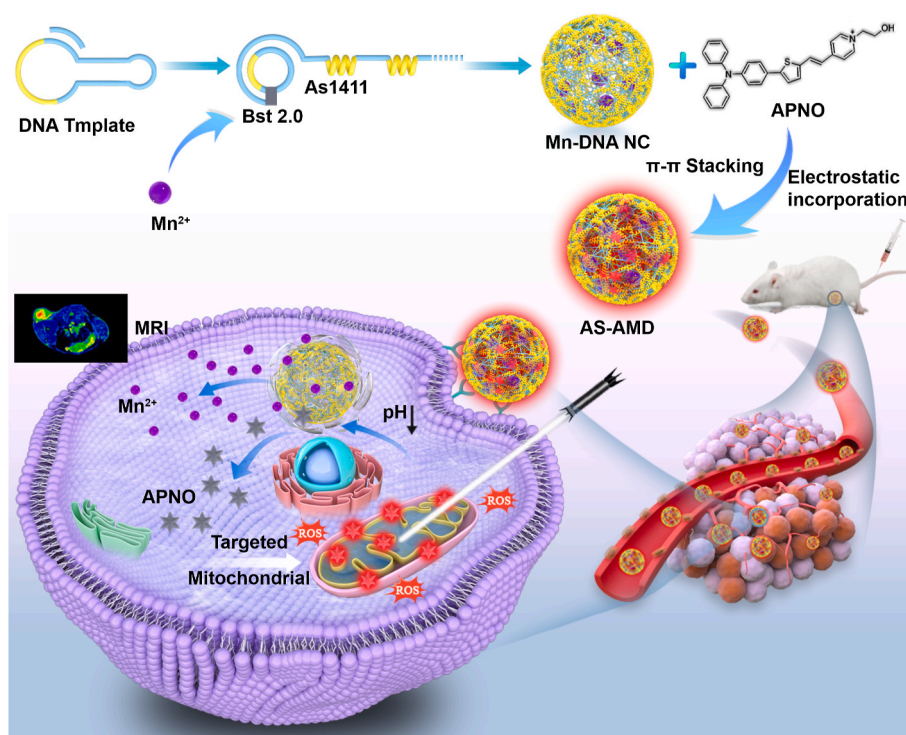

Fig. 1. Schematic illustration of poly AS1411 aptamer-encoded DNA nanoclew for tumor site activated mitochondria-targeted PDT and MRI.

centrifuged at 10000 rpm for 10 min, and repeated twice. The product in the ultrafiltration tube was sucked out and stored at 4 °C. The loading contents of APNO was 7.3 %. The loading efficiency was 86.4 %. The content of Mn in AS-AMD was determined to be 10.5 % using Inductively Coupled Plasma Mass Spectrometry (ICP-MS).

2.4. Cell uptake

4T1 cells were seeded in confocal culture dishes at a density of 10,000 cells per dish. After 24 h incubation, 4T1 cells were incubated with AS-AMD or AMD (APNO concentration: 2 μM) for 2 h. Cellular uptake was determined by CLSM (Leica STELLARIS 5, Germany) and flow cytometry analysis.

2.5. Mitochondrial imaging

Cells were inoculated into confocal dishes at a density of 10,000 cells per dish. After 24 h of incubation, AS-AMD (APNO concentration: 2 μM) was added to the cells. Following a 2 h incubation period, the supernatant was discarded, and the cells were rinsed with PBS. Then the cells were stained with MitoTracker Green and observed by CLSM.

2.6. Cellular ROS detection

To assess intracellular ROS production of AS-AMD, 4T1 cells were seeded into 12-well plates. Samples were added and incubated for 2 h. Then the cells were stained with DCFHDA at 37 °C for 0.5 h. After white light irradiation for 5 min (50 mW cm^{-2}), green fluorescence was observed using a fluorescence inverted microscope.

2.7. In vivo MRI

All animal experiments were carried out according to the Principles of Laboratory Animal Care of the People's Republic of China and the Guidelines for the Care and Use of Laboratory Animals of Xuzhou Medical University, China (Permission No. 202302T005). Subcutaneous implantation of 1×10^6 4T1 cells in mice for tumor model.

4T1 tumor-bearing mice were selected to evaluate T_1-weighted imaging performance of AS-AMD. Three mice in the experimental group were intravenous injected with 200 μL of AS-AMD sample (Mn^{2+} concentration: 5 mM). The other 3 mice were injected with the same amount of AMD sample as a control group. T1-weighted MRI images were acquired using a 3.0T MRI system at 0 h, 2 h, 4 h, 8 h, 12 h and 24 h of postinjection, respectively. The tumor T_1 signal intensity was analyzed to evaluate the MRI performance. All mice were sacrificed after imaging for biodistribution study and assayed by ICP-MS. The percent of injected dose/gram of tissue (% ID/g) was then calculated.

2.8. In vivo anticancer effect

For *in vivo* antitumor efficacy, a 4T1 tumor model was established in the same manner as described in the *in vivo* imaging section. When the tumor volume reached ≈100 mm^3, mice were randomly divided into six groups (n = 5): PBS without light, PBS with light, AMD without light (5 mg kg^{-1}), AMD with light, AS-AMD without light, and AS-AMD with light (APNO dose: 5 mg/kg). Mice bearing 4T1 tumors were exposed to white light for 10 min (150 mW cm^{-2}) after intravenous injection of samples at 4 h post-injection. The dimensions of the tumors were measured every two days, and the tumors volume was calculated using the formula: volume = (length of the tumors) × (width of the tumors)^2/2.

2.8.1. Other experiment procedures

For detailed experimental protocols, please consult the supplementary information.

3. Results and discussion

3.1. Preparation and characterization of AS-AMD

DNA nanoclew was synthesized by RCA reaction-induced assembly, and the RCA DNA templates were designed by encoding the complementary AS1411 aptamer sequence (sequences are shown in Table S1). The assembly of RCA products was verified by agarose gel electrophoresis. According to Fig. S1, the RCA products bands moved to higher sites compared to the circle DNA template (CT), which was attributed to the larger-sized DNA nanoclew obtained from self-assembly by the RCA reaction. These results indicated that the polynucleotide with AS1411 aptamer has been successfully synthesized. The mitochondria-targeted PSs APNO was synthesized according to our previous report [28], which was confirmed by NMR (Fig. S2). APNO exhibited obvious AIE features by investigating the fluorescence changes in different ratios of toluene (Fig. S3). The cation APNO was then embedded in the DNA nanoclew by π-π stacking and electrostatic incorporation to obtain multifunctional DNA nanoclew (AS-AMD). The fluorescence intensity gradually strengthened with the increase of DNA concentration, which demonstrated that APNO was successfully embedded in the DNA structure leading to the generation of fluorescence (Fig. S4). The morphology and elemental distribution of AS-AMD were characterized by scanning electron microscopy (SEM), transmission electron microscopy (TEM), and energy-dispersive X-ray spectroscopy (STEM-EDS), where the formation of spherical morphology and the homogeneous distribution of C, N, P, and Mn elements were observed (Fig. 2A–C). In addition, the particle size of AS-AMD was about 275 ± 16 nm determined by the dynamic light scattering (DLS). Furthermore, the particle size of AS-AMD exhibited remarkable stability, with no significant change within 14 days, confirming its excellent stability (Fig. S5).

As illustrated in Fig. 2E, similar to APNO and DNA nanoclew, the AS-AMD exhibited characteristic absorption bands of APNO and DNA at 465 nm and 254 nm, respectively, in their UV–Vis spectra, indicating the efficient intercalation of APNO within the DNA nanoclew structure. Compared to DNA nanoclew, the zeta potential of AS-AMD was increased from −14.9 mV to −10.3 mV, which further confirmed the successful insertion of the APNO (Fig. S6). The pH-responsive release behavior of APNO-loaded AS-AND was subsequently investigated. The release of APNO under different pH conditions was recorded by the UV–Vis spectrophotometer, and it was found that only a negligible amount of APNO was released under neutral conditions at pH 7.4. Interestingly, drug release was accelerated with decreasing pH. At pH 6.5 and pH 6.0, 26.2 % and 47.5 % of APNO was released within 24 h, respectively. While at the more acidic pH 5.5, more than 70 % of APNO was released within 24 h. The fluorescence of the released AIE photosensitizer APNO will decrease or even disappear due to its monomolecular state. The release behavior of APNO was also explored by detecting fluorescence changes of AS-AMD. After co-incubation with solutions of different pH for 0.5 h, the AS-AMD solution at pH 5.5 exhibited the weakest fluorescence intensity, indicating that more APNO was released (Fig. S7). This behavior enables the rapid release of APNO from AS-AMD after cellular uptake, facilitating subsequent mitochondrial targeting.

The *in vitro* production of ROS by AS-AMD was quantified utilizing a SOSG (Singlet Oxygen Sensor Green) fluorescent probe. SOSG (final concentration, 5 μM) was dissolved in PBS, DNA nanoclew (not loaded with APNO) and AS-AMD (containing 1 μg/ml APNO) were mixed and exposed to light irradiation (50 mW cm^{-2}) for 5 min. Fluorescence intensity was measured using a fluorescence spectrometer (Ex/Em = 504/525 nm). As depicted in Fig. S8, the fluorescence intensity of SOSG treated with AS-AMD exhibited approximately a 7-fold increase post-light irradiation compared to the PBS-only group. This significant enhancement confirms the capability of AS-AMD to generate ROS upon activation by light, thereby highlighting its potential as a PDT agent.
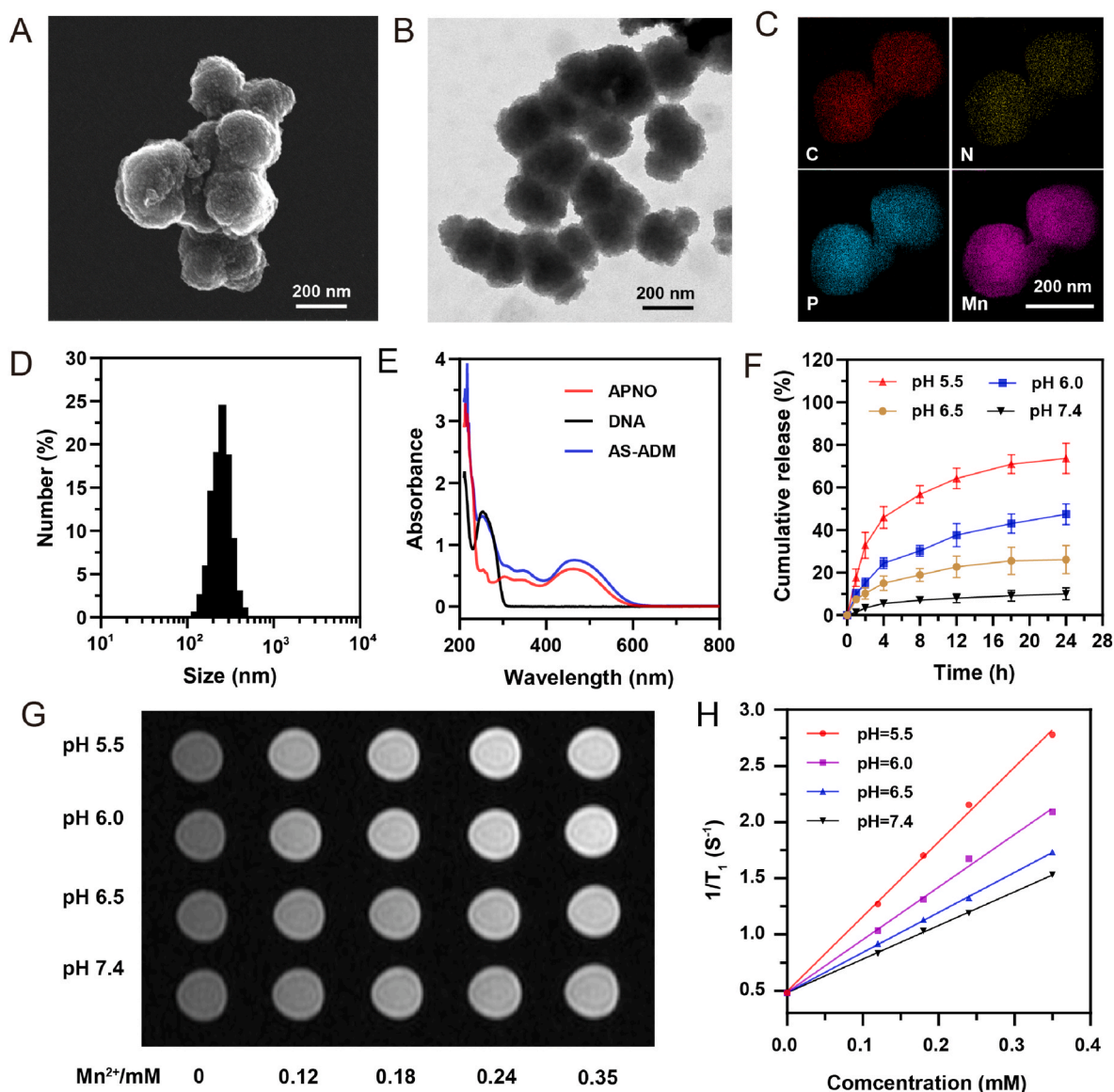
Fig. 2. A) SEM and B)TEM images of AS-AMD. C) The elemental mappings of C, N, P, and Mn in AS-AMD. D) Particle size of AS-AMD determined by DLS. E) UV–Vis spectra of APNO, DNA, and AS-AMD. F) *In vitro* release behavior of APNO from AS-AMD at pH 5.5, 6.0, 6.5, and 7.4. G) T_1-weighted MR images of AS-AMD at pH 5.5, 6.0, 6.5, and 7.4. H) Transverse relaxation rates of AS-AMD at pH 5.5, 6.0, 6.5, and 7.4.

3.2. T_1 longitudinal relaxivity of AS-AMD

After released from the nanoparticles, paramagnetic Mn^{2+} can form strong coordination bonds with nearby protons, thereby, improving MRI performance [29]. Mn^{2+} during the RCA reaction not only acted as a cofactor to catalyze the elongation of single-stranded DNA, but also serveed as the framework of DNA nanoclew. In an acidic environment, AS-AMD will decompose to release free Mn^{2+}, thereby enhancing MRI performance [30]. First, the release profiles of Mn^{2+} from AS-AMD at different pH PBS buffesr (pH 5.5, pH 6.0, pH 6.5 and pH 7.4) were measured by ICP-MS. As shown in Fig. S9, only 20.2 % of Mn^{2+} was released from AS-AMD within 24 h, while the rapid release of Mn was observed under acidic conditions at pH 6.5, pH 6.0, and pH 5.5, accounting for 59.7 %, 76.9 %, and 87.1 %, respectively. Then T_1-weighted MR phantom images of AS-AMD in different pH PBS buffers were detected with a 3T MR scanner. As illustrated in Fig. 2G, AS-AMD in the acidic condition (pH 6.5, pH 6.0, and pH 5.5) exhibited a brighter signal compared to pH 7.4. Then we analyzed the transverse relaxation rate ($1/T_1$) of AS-AMD with different pH to give the longitudinal MR

relaxation rate (r_1, $r_1 = \Delta(1/T_1)/\Delta[Mn^{2+}]$) values. As shown in Fig. 2H, the r_1 relaxivity of AS-AMD at pH 7.4 was 2.99 mM^{-1} s^{-1}. At pH 6.5 and pH 6.0, the r_1 relaxivity increased to 3.56 mM^{-1} s^{-1} and 4.68 mM^{-1} s^{-1}, respectively. Moreover, the r_1 relaxivity increased to 6.65 mM^{-1} s^{-1} at pH 5.5, which was 2.2 times enhancement than at pH 7.4. Acidic environment inducing a higher relaxation rate of AS-AMD enabled tumor sites to exhibit enhanced MRI signals in the acidic microenvironment.

3.3. Specific cell-targeting and MRI of AS-AMD

Further in vitro cellular MRI was performed to evaluate the specific cell-targeting ability of AS-AMD and its potential for MRI of tumor cells. Fibroblasts (NIH/3T3) and breast tumor cells (4T1) were co-incubated with different concentrations of AS-AMD. As seen in Fig. S10, the MRI signal intensity of 4T1 cells was gradually enhanced with increasing Mn^{2+} concentration. As a comparison, NIH/3T3 cells co-cultured with AS-AMD only exhibited weak MRI signals. The MRI signal intensity of 4T1 cells co-incubated with AS-AMD was almost 4.2-fold of the signal of NIH/3T3 cells at a Mn^{2+} concentration of 0.5 mM, indicating the specific

targeting ability of the AS-AMD. The specific targeting ability to 4T1 cells was mainly attributed to the specific recognition by AS1411 integrated in AS-AMD of nucleolin highly expressed on tumor cell membranes.

3.4. Cell uptake and mitochondrial imaging of AS-AMD

To demonstrate the enhancing cell uptake, nanoclew (AMD) without AS1411 aptamer were also synthesized by RCA polymerization to serve as a control. Then AMD or AS-AMD was incubated with 4T1 cells for 0.5 h, 1 h, and 2 h, respectively, and subsequently imaged by confocal laser scanning microscope (CLSM). As depicted in Fig. 3A, a more pronounced red fluorescence is evident in 4T1 cells treated with AS-AMD, suggesting that the integration of the poly-AS1411 aptamer significantly enhances the DNA nanoclew's targeting prowess and cellular uptake within 4T1 tumor cells. Quantitative fluorescence analysis of single cell was then performed (Fig. 3B), and it was found that the fluorescence intensity of tumor cells treated by AS-AMD was approximately 2-fold higher than AMD-treated 4T1 cells at the same incubation time. Enhanced cellular uptake was further verified by flow cytometry. As shown in Fig. S11, AS-AMD-treated 4T1 cells showed stronger fluorescence, which was also consistent with the results of fluorescent images by CLSM. These results

demonstrated enhanced cellular uptake of AS-AMD to 4T1 cells due to the high affinity of the AS1411 aptamer for tumor cells. To further verify the selectivity of AS-AMD for tumor cells with high expression of nucleolin, NIH/3T3 cells were co-cultured with AS-AMD for 2 h. As shown in Fig. S12, the fluorescence intensity of 4T1 cells exceeded that of NIH/3T3 cells by more than two times, confirming the high degree of specificity exhibited by AS-AMD for targeting tumor cells over normal cell lines.

To investigate the intracellular behavior of AS-AMD, CLSM was used to study the mitochondrial targeting ability of APNO. After the coincubation of 4T1 cells with APNO and MitoTracker Green for 0.5 h, the fluorescence co-localization was observed. As shown in Fig. S13, the red fluorescence of APNO could overlap well with the green fluorescence of MitoTracker Green, indicating the mitochondrial targeting of APNO. Then, the mitochondria-targeted delivery capacity of AS-AMD was further investigated in 4T1 cells. 4T1 cells were incubated with AS-AMD for 2h and then stained using MitoTracker Green or Lyso Tracker Green. Compared to Lyso Tracker Green, the red fluorescence of APNO could better cover the green fluorescence of MitoTracker Green(Fig. 3C–F). Moreover, the Pearson correlation coefficients Rr of the red fluorescence with the green fluorescence of Mito Tracker Green was as high as 0.97, indicating that APNO released from AS-AMD was localized in
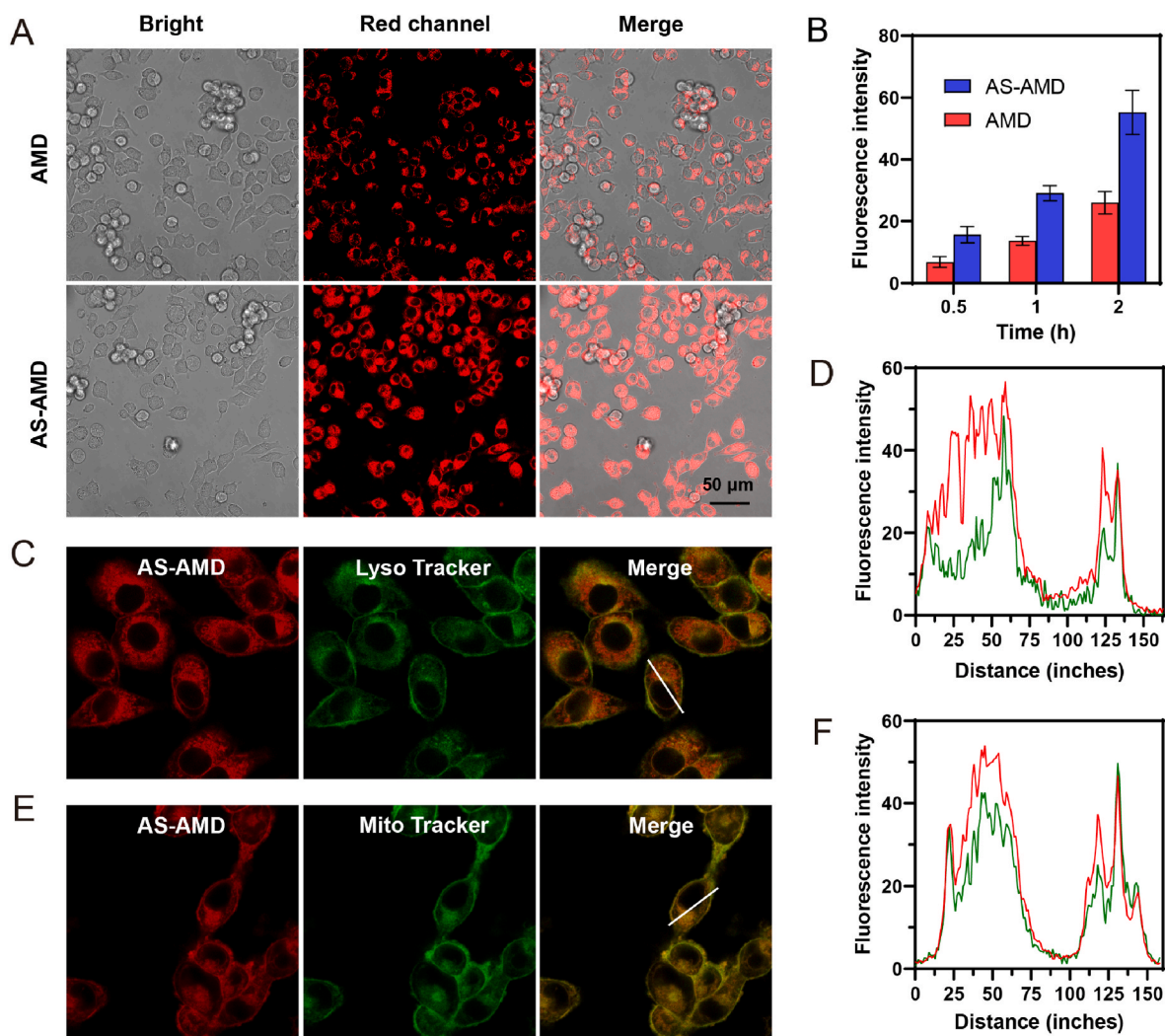

Fig. 3. A) Confocal images of 4T1 cells after incubation with AMD or AS-AMD for 2 h (APNO concentration: 2 μM). Scale bar: 50 μm. B) Mean fluorescence intensity of a single 4T1 cell for different incubation time. C) Confocal images of 4T1 cells after incubation with AS-AMD and MitoTracker Green (APNO concentration: 2 μM). Scale bar: 50 μm. D) Colocalization linear analyses on the fluorescence of 4T1 cells. (For interpretation of the references to colour in this figure legend, the reader is referred to the Web version of this article.)

mitochondria (Fig. S14). Mitochondria-targeted delivery of APNO by DNA nanoclew provides the possibility for further mitochondria-targeted PDT.

3.5. Cell biocompatibility and ROS generation

Before AS-AMD was used for further cellular PDT, biocompatibility was first exploited on NIH/3T3 and TC-1 breast epithelial cells by CCK-8 assay. As illustrated in Fig. S15, both NIH/3T3 and TC-1 maintained a high viability higher than 90 % after 24 h of co-incubation with AS-AMD, suggesting that AS-AMD has only negligible toxicity to the cells.

The hemocompatibility of AS-AMD was further investigated by examining the hemolysis outcomes of erythrocytes with deionized water, PBS, and different concentrations of AS-AMD solutions. As depicted in Fig. S16, no significant appearance of hemolysis was observed in PBS and all AS-AMD-treated erythrocytes compared to DI water. Even when the concentration of AS-AMD was 300 μg/mL, the rate of hemolysis was still found to be less than 5 %. The excellent biocompatibility of AS-AMD offers promise for further biomedical applications.

To demonstrate the intracellular ROS-generating properties of APNO-loaded AS-AMD, 4T1 cells were treated with AS-AMD and then stained by 2′,7′-dichlorofluorescin diacetate (DCFHDA), a commercial
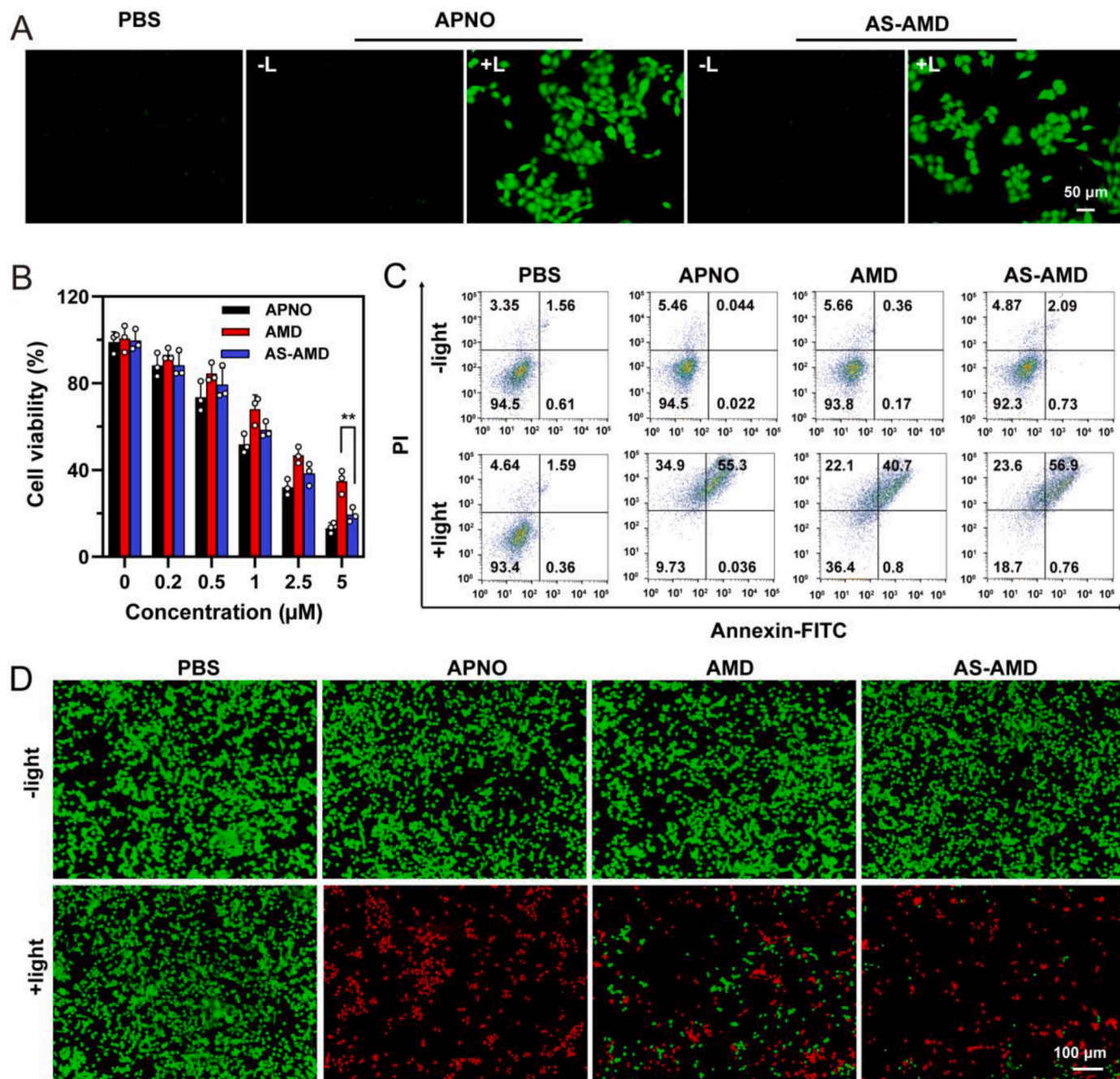

Fig. 4. A) Fluorescence images of 4T1 cells stained with DCFHDA to study cellular ROS production. Scale bar: 50 μm. B) Viability of 4T1 cells after treatment with different concentrations of APNO, AMD or AS-AMD under light irradiation. Error bars indicated SD (n = 3). **P < 0.01 (t-test). C) Apoptotic effect of 4T1 cells treated with PBS, APNO, AMD, or AS-AMD under dark or light irradiation determined by the Annexin V-FITC/PI assay through flow cytometry. D) Fluorescence images of live cells (green) and dead cells (red) treated with with PBS, APNO, AMD, or AS-AMD under dark or light irradiation. Scale bar: 100 μm. (For interpretation of the references to colour in this figure legend, the reader is referred to the Web version of this article.)

fluorescent probe for ROS detection. 4T1 cells incubated for 2 h with APNO and APNO-loaded AS-AMD irradiated with light irradiation for 5 min exhibited a very distinct green fluorescence, suggesting effective ROS were produced (Fig. 4A and S17). Meanwhile, very little fluorescence was observed in the PBS group and the group without light exposure. These results suggested that under light irradiation AS-AMD could produce efficient ROS, which could be employed for further tumor PDT.

3.6. In vitro PDT

Cytotoxicity and phototoxicity of APNO, AMD, and AS-AMD were assessed by CCK-8 assay. APNO, AMD, and AS-AMD all exhibited negligible cytotoxicity in the absence of light, indicating that no cytotoxic ROS were produced under dark conditions (Fig. S18). APNO, AMD and AS-AMD all exhibited concentration-dependent cytotoxicity under light irradiation. As can be seen from Fig. 4B, when the concentration of

APNO was 5 μM, the cell viability of AMD-treated 4T1 cells was decreased to 34.8 %, whereas the cell viability of AS-AMD-treated 4T1 cells was decreased to 14.6 %. The enhanced cytotoxicity of AS-AMD was attributed to the modification of AS1411 to promote cellular uptake of DNA nanoclew.

Apoptosis analysis of PDT-treated cells was performed by a flow cytometry system after annexin V-TITC/propidium iodide (PI) double staining. As presented in Fig. 4C and S19, more than 92 % of the cells in the PBS ± light group, APNO, AMD, and AS-AMD without light groups, were distributed in the lower left quadrant, indicating that these treated cells exhibited good survival. However, the apoptosis and necrosis rate of AMD-treated cells reached 63.6 % after light irradiation, which was a consequence of apoptosis induced by light-generated ROS in tumor cells. What's more, the apoptosis and necrosis rate of AS-AMD treatment was significantly increased to 81.3 % due to higher cellular uptake. Additionally, the enhanced PDT of AS-AMD was further demonstrated by live-dead cell staining analysis. As demonstrated in Fig. 4D, T1 cells co-
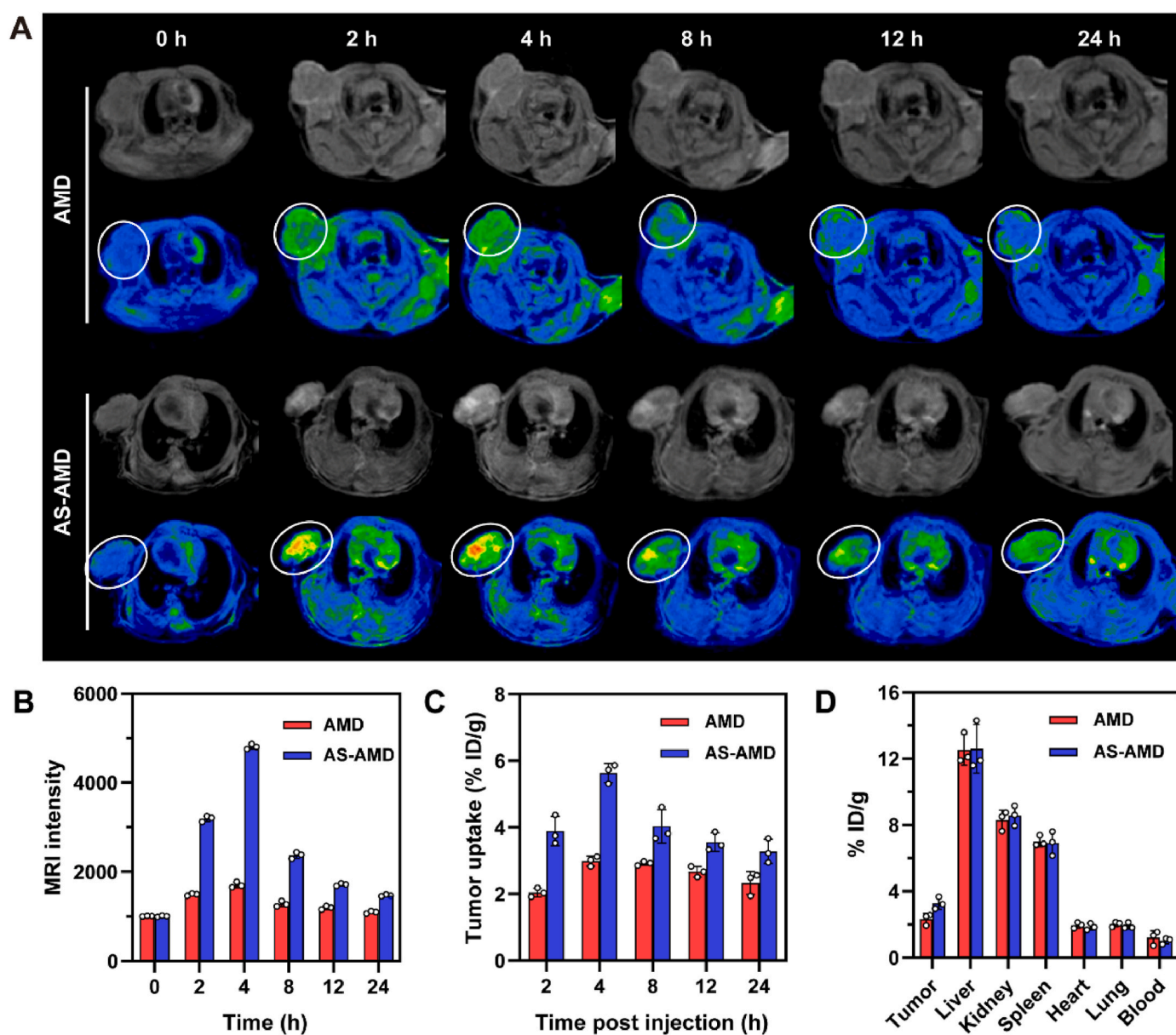

Fig. 5. A) *In vivo* T_1-wighted MR imaging of 4T1-tumor-bearing mice after intravenous injection of with AMD and AS-AMD, respectively. B) T_1-wighted MRI signals of tumors at different time points after intravenous injection of with AMD and AS-AMD. C) Tumor uptake of AMD and AS-AMD at different time points. D) Biodistribution of tumor and primary organs after 24 h injection.

treated with light and AS-AMD exhibited an increase in red fluorescence and a concomitant decrease in green fluorescence, suggesting that the application of AS-AMD subsequent to laser irradiation resulted in significantly augmented cytotoxicity.

Since the released APNO from AS-AMD can target mitochondria, mitochondrial damage was assessed by detecting mitochondrial membrane potential (MMP). JC-1 dye was used as an indicator to assess the depolarization of MMP. As depicted in Fig. S20A, distinct green fluorescence was observed in 4T1 cells treated with AS-AMD + L, whereas cells in other groups exhibited pronounced red fluorescence. This observation indicated that irradiation of AS-AMD induced significant mitochondrial depolarization, leading to the transition of JC-1 from aggregate to monomeric state. Flow cytometry analysis results further verified the changes in MMP after irradiation (Fig. S20B).

3.7. In vivo MRI and distribution

In vivo T_1-weighted MRI of AS-AMD was then performed on 4T1-tumor-bearing mice. 4T1-tumor-bearing mice injected nonAS1411-embedded AMD nanoclew were served as a control group. MRI images of the mice were gathered by the MRI system at determined time points

to assess imaging properties. As presented in Fig. 5A, after injection of AS-AMD, the T_1-weighted MR signals in the tumor sites were gradually enhanced, and the signals reached a maximum after 4 h. Meanwhile, mice injected with AMD showed weaker MR signals at tumor sites. The MR signal intensity at the tumor site of mice injected with AS-AMD was 2.82-fold higher than that injected with AMD at 4 h postinjection (Fig. 5B). This enhanced MRI signal at the tumor site was mainly attributed to the enhanced tumor targeting of DNA nanoclew by AS1411 aptamer. The efficient tumor-targeting ability of AS-AMD was further confirmed by *in vivo* fluorescence imaging studies performed in mice models. As depicted in Fig. S21, a substantial escalation in fluorescent signal intensity at the tumor site was discerned following intravenous administration, thereby affirming the selective accumulation of AS-AMD within the malignant tissues and validating its tumor-targeting precision.

Tumor uptake and primary organs distribution of AS-AMD were further investigated, which were measured by inductively coupled plasma mass spectrometry (ICP-MS). As demonstrated in Fig. 5C, after injection of DNA nanclew, tumor uptake was at a maximum of 4 h and then gradually eliminated. The tumor uptake of AS-AMD was calculated to be 5.63 ± 0.32 % at 4 h postinjection, compared to only 2.99 ± 0.16
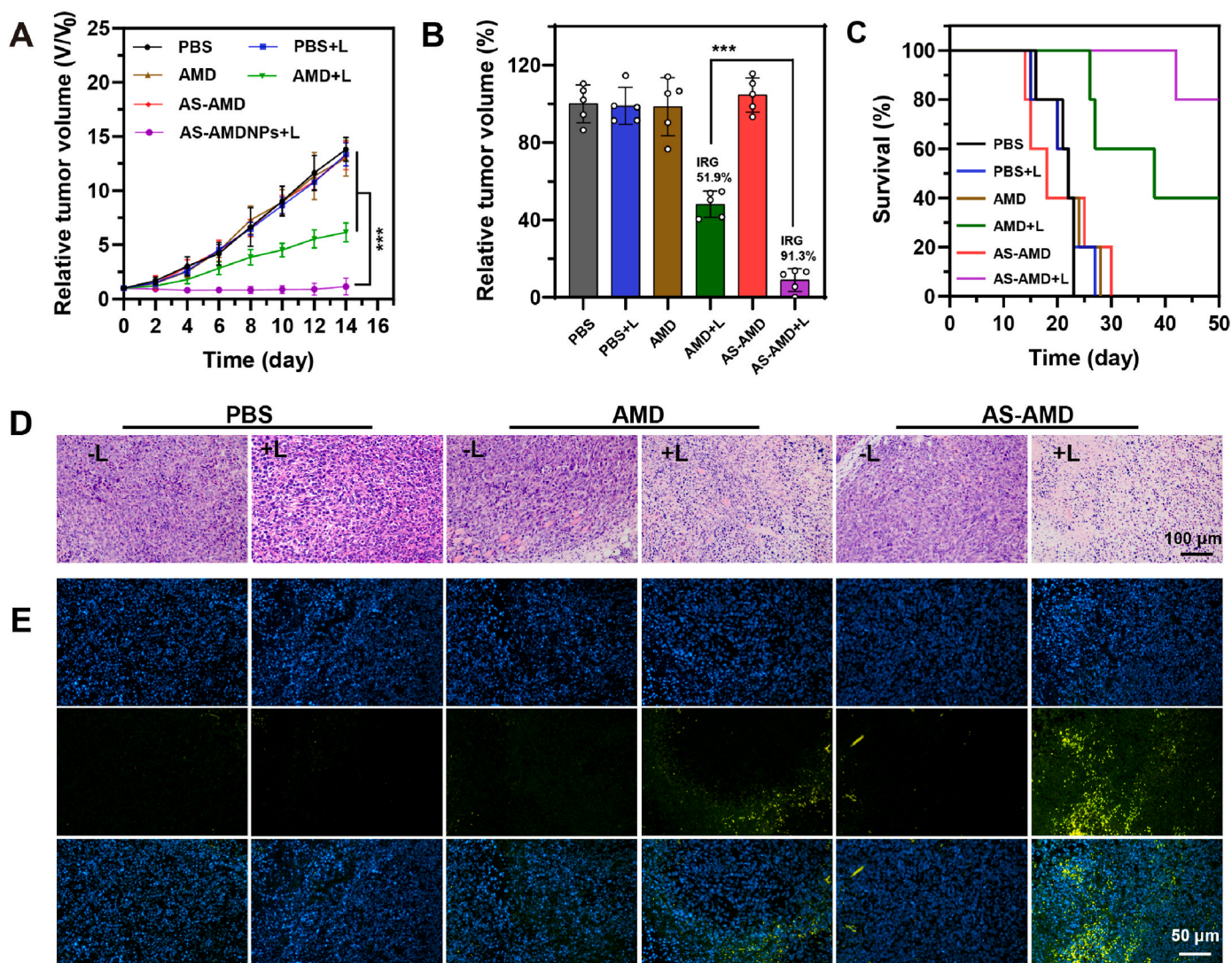

Fig. 6. A) Relative tumor volumes of 4T1-tumor-bearing mice treated with different samples. Error bars indicated SD (n = 5). ***P < 0.001 (t-test). B) The inhibition rate of tumor growth (IRG) after 14 days' therapy. Error bars indicated SD (n = 5). ***P < 0.001 (t-test). C). The survival rates of mice following various treatments. D) Tumor tissues stained with hematoxylin and eosin after 14 days' therapy. Scale bar: 100 μm. E) TUNEL-stained tumor slices collected from mice after 14 days' therapy. Scale bar: 50 μm.

% for AMD. This enhanced tumor uptake of AS-AMD was primarily a consequence of tumor targeting of AS1411 aptamer as well as the prolonged blood circulation (Fig. S22). Mice were sacrificed at 24 h post-injection. AS-AMD was found to maintain favorable tumor accumulation and retention by the measured ex vivo biodistribution results (Fig. 5D), which was also consistent with the MRI results.

3.8. In vivo anticancer effect

Further *in vivo* PDT anti-tumor research was then performed in 4T1-tumor-bearing mice. When the tumors reached approximately 100 mm^3, 30 4T1-tumor-bearing mice were randomly divided into 6 groups: (1) control group injected with PBS, (2) injection with PBS plus light, (3) only injection with AMD, (4) injection with AMD plus light, (5) only injection with AS-AMD, and (5) injection with AS-AMD plus light. Tumors were exposed to 150 mW cm^{-2} light for 10 min. Tumor size was assessed every 48 h to evaluate the efficacy of PDT. Significant tumor growth inhibition was achieved in the AMD and AS-AMD with light irradiation groups compared to the saline-treated control and without light irradiation groups (Fig. 6A and S23). Importantly, the AS-AMD with light irradiation group showed the best antitumor effects. On the 14th day, the relative tumor volumes and the inhibition rates of tumor growth (IRG) for the various groups were determined. As seen in Fig. 6B and S24, the IRG of the AS-AMD plus light group was as high as 91.3 %, surpassing the rate observed in the AMD plus light group (51.9 %). Moreover, Mice treated with AS-AMD exhibited a significant extension in survival (Fig. 6C).

To further validate the enhanced effect of PDT, histological examinations using hematoxylin and eosin (H&E) and terminal deoxynucleotidyl transferase-mediated dUTP-biotin nick-end labeling (TUNEL) staining assays were performed on tumor tissue slices obtained from different treatment groups to assess the destruction of tumor cells. Apoptotic cells show green fluorescence in combination with the green fluorescent probe FITC-labeled dUTP, while normal cells do not fluoresce. Fig. 6D and E revealed that tumors treated with AS-AMD plus light displayed notable nuclear fragmentation and the most extensive tissue necrosis. The enhanced antitumor effect of AS-AMD was primarily attributed to the efficient mitochondria-targeted delivery of APNO PSs by poly-AS 1411 aptamer DNA nanoclew.

Additionally, there was no observed decrease in body weight of mice throughout the treatment period (Fig. S25). To further examine the biocompatibility of AS-AMD, major organs (liver, spleen, kidneys, heart, and lungs) were harvested from AS-AMD-treated mice at 14 days post-injection and sliced for H&E staining. As demonstrated in Fig. S26, no significant abnormalities were evident in the major tissues of mice after various treatments. These findings suggested that the synthesized DNA nanoclew possessed high biocompatibility and safety for *in vivo* imaging and cancer treatment, paving the way for potential clinical applications.

4. Conclusion

In conclusion, a poly-AS1411 aptamer -encoded DNA nanoclew inserted with cationic PSs (APNO) and paramagnetic Mn^{2+} was developed for enhanced MRI and image-guided mitochondria-targeted PDT. The synthesized AS-AMD showed effective tumor accumulation, which was attributed to the tumor-specific targeting and increased internalization by tumor cells mediated by encoded AS1411 aptamer. In the acidic tumor microenvironment, paramagnetic Mn^{2+} was released from AS-AMD, achieving enhanced T$_1$-weighted MRI and guiding subsequent tumor therapy. Following AS-AMD enters the acidic endosome, APNO was released and targets the mitochondrial membrane, achieving mitochondria-targeted delivery of cationic PSs. Under light irradiation, APNO generated cytotoxic ROS, achieving mitochondria-targeted PDT. Therefore, this synthesized AS-AMD contributed a novel strategy to achieve mitochondria-targeted delivery of PSs and the development of nanotheranostic agents based on DNA nanotechnology. Furthermore,

the aptamer-encoded DNA nanotechnology delivery system offers a mitochondria-targeted PDT platform strategy that can be adapted to target alternative diseases by modifying the sequence design of the complementary aptamer region within the DNA template.

CRediT authorship contribution statement

Minghui Chen: Writing – original draft, Validation, Formal analysis, Conceptualization. **Hanbo Xu:** Methodology, Investigation, Data curation. **Pengzhao Chang:** Methodology, Data curation. **Xueqi Li:** Methodology. **Shuang Liu:** Validation, Investigation. **Lingyue Xu:** Validation, Investigation. **Kai Xu:** Project administration, Funding acquisition. **Guohui Cheng:** Writing – review & editing, Supervision, Project administration, Funding acquisition.

Ethics approval and consent to participate

All animal experiments were conducted according to the Principles of Laboratory Animal Care of the People's Republic of China and the Guidelines for the Care and Use of Laboratory Animals of Xuzhou Medical University, China (Permission No. 202302T005).

Declaration of competing interest

The authors declare the following financial interests/personal relationships which may be considered as potential competing interests: The work has not been submitted elsewhere for publication, in whole or in part, and all the authors listed have approved the manuscript that is enclosed.

Acknowledgements

Appendix A. Supplementary data

Supplementary data to this article can be found online at https://doi.org/10.1016/j.mtbio.2024.101318.

Data availability

No data was used for the research described in the article.

References

[1] D.E.J.G.J. Dolmans, D. Fukumura, R.K. Jain, Photodynamic therapy for cancer, Nat. Rev. Cancer 3 (5) (2003) 380–387.

[2] P. Agostinis, K. Berg, K.A. Cengel, T.H. Foster, A.W. Girotti, S.O. Gollnick, S.M. Hahn, M.R. Hamblin, A. Juzeniene, D. Kessel, M. Korbelik, J. Moan, P. Mroz, D. Nowis, J. Piette, B.C. Wilson, J. Golab, Photodynamic therapy of cancer: an update, Ca-Cancer J Clin 61 (4) (2011) 250–281.

[3] S. Son, J. Kim, J. Kim, B. Kim, J. Lee, Y. Kim, M.L. Li, H. Kang, J.S. Kim, Cancer therapeutics based on diverse energy sources, Chem. Soc. Rev. 51 (19) (2022) 8201–8215.

[4] N. Rabiee, M.T. Yaraki, S.M. Garakani, S.M. Garakani, S. Ahmadi, A. Lajevardi, M. Bagherzadeh, M. Rabiee, L. Tayebi, M. Tahriri, M.R. Hamblin, Recent advances in porphyrin-based nanocomposites for effective targeted imaging and therapy, Biomaterials 232 (2020) 119707.

[5] J.Z. Zhao, W.H. Wu, J.F. Sun, S. Guo, Triplet photosensitizers: from molecular design to applications, Chem. Soc. Rev. 42 (12) (2013) 5323–5351.

[6] J. Zielonka, J. Joseph, A. Sikora, M. Hardy, O. Ouari, J. Vasquez-Vivar, G. Cheng, M. Lopez, B. Kalyanaraman, Mitochondria-targeted triphenylphosphonium-based

compounds: syntheses, mechanisms of action, and therapeutic and diagnostic applications, Chem. Rev. 117 (15) (2017) 10043–10120.

[7] L.M. Yang, P. Gao, Y.L. Huang, X. Lu, Q. Chang, W. Pan, N. Li, B. Tang, Boosting the photodynamic therapy efficiency with a mitochondria-targeted nanophotosensitizer, Chin. Chem. Lett. 30 (6) (2019) 1293–1296.

[8] Y. Yamada, H. Harashima, Mitochondrial drug delivery systems for macromolecule and their therapeutic application to mitochondrial diseases, Adv Drug Deliver Rev 60 (13–14) (2008) 1439–1462.

[9] X.Y. Long, M. Liu, Y.Y. Nan, Q.H. Chen, Z.X. Xiao, Y.T. Xiang, X.H. Ying, J. Sun, Q. Huang, K.L. Ai, Revitalizing ancient mitochondria with nano-strategies: mitochondria-remedying nanodrugs concentrate on disease control, Adv. Mater. 36 (18) (2024) 2308239.

[10] W.J. Sun, J.Q. Wang, Q.Y. Hu, X.W. Zhou, A. Khademhosseini, Z. Gu, Crispr-cas12a delivery by DNA-mediated bioresponsive editing for cholesterol regulation, Sci. Adv. 6 (21) (2020) eaba2983.

[11] W.J. Sun, T.Y. Jiang, Y. Lu, M. Reiff, R. Mo, Z. Gu, Cocoon-like self-degradable DNA nanoclew for anticancer drug delivery, J. Am. Chem. Soc. 136 (42) (2014) 14722–14725.

[12] H.F. Ji, Q.B. Zhu, Application of intelligent responsive DNA self-assembling nanomaterials in drug delivery, J. Controlled Release 361 (2023) 803–818.

[13] K. Li, Y.F. Liu, B.B. Lou, Y.F. Tan, L.W. Chen, Z.B. Liu, DNA-directed assembly of nanomaterials and their biomedical applications, Int. J. Biol. Macromol. 245 (2023) 125551.

[14] A.S.G. Martins, S.D. Reis, E. Benson, M.M. Domingues, J. Cortinhas, J.A.V. Silva, S. D. Santos, N.C. Santos, A.P. Pêgo, P.M.D. Moreno, Enhancing neuronal cell uptake of therapeutic nucleic acids with tetrahedral DNA nanostructures, Small (2024) 2309140.

[15] A. Lacroix, H.F. Sleiman, DNA nanostructures: current challenges and opportunities for cellular delivery, ACS Nano 15 (3) (2021) 3631–3645.

[16] Y. Hu, Z. Chen, H. Zhang, M.K. Li, Z. Hou, X.X. Luo, X.Y. Xue, Development of DNA tetrahedron-based drug delivery system, Drug Deliv. 24 (1) (2017) 1295–1301.

[17] K. Xu, Y.W. Du, B.Y. Xu, Y.Q. Huang, W. Feng, D.H. Yu, Y. Chen, X.L. Wang, Gelatin-encapsulated Tetrahedral DNA Nanostructure Enhances Cellular Internalization for Treating Noise-Induced Hearing Loss, Small, 2024 2310604.

[18] T.R. Tian, T. Zhang, S.R. Shi, Y. Gao, X.X. Cai, Y.F. Lin, A dynamic DNA tetrahedron framework for active targeting, Nat. Protoc. 18 (4) (2023) 1028–1055.

[19] X. Luo, D. Saliba, T.X. Yang, S. Gentile, K. Mori, P. Islas, T. Das, N. Bagheri, A. Porchetta, A. Guarne, G. Cosa, H.F. Sleiman, Minimalist design of wireframe DNA nanotubes: tunable geometry, size, chirality, and dynamics, Angew. Chem. Int. Ed. 62 (44) (2023) e202309869.

[20] Y. Yang, W.J. Zhu, L.Z. Feng, Y. Chao, X. Yi, Z.L. Dong, K. Yang, W.H. Tan, Z. Liu, M.W. Chen, G-quadruplex-based nanoscale coordination polymers to modulate tumor hypoxia and achieve nuclear-targeted drug delivery for enhanced photodynamic therapy, Nano Lett. 18 (11) (2018) 6867–6875.

[21] C.C. Li, Y.S. Gao, Q. Li, S.S. Luo, W.Q. Liao, Z.S. Wu, Adhesive aunp tape-mediated hierarchical assembly of multicenter DNA nanocomplexes for tumor cell nucleus-targeted staged drug delivery in vivo, Nano Today 47 (2022) 101687.

[22] R.Y. Yue, M.J. Zhou, X. Li, L. Xu, C. Lu, Z. Dong, L.L. Lei, H.Y. Liu, G.Q. Guan, Q. Liu, X.B. Zhang, G.S. Song, Gsh/ape1 cascade-activated nanoplatform for imaging therapy resistance dynamics and enzyme-mediated adaptive ferroptosis, ACS Nano 17 (14) (2023) 13792–13810.

[23] D.Y. Wang, H. Yi, S.Z. Geng, C.M. Jiang, J.W. Liu, J. Duan, Z.Z. Zhang, J.J. Shi, H. W. Song, Z.Z. Guo, K.X. Zhang, Photoactivated DNA nanodrugs damage mitochondria to improve gene therapy for reversing chemoresistance, ACS Nano 17 (17) (2023) 16923–16934.

[24] H.X. Zhao, L.H. Li, F. Li, C.X. Liu, M.X. Huang, J. Li, F. Gao, X.H. Ruan, D.Y. Yang, An energy-storing DNA-based nanocomplex for laser-free photodynamic therapy, Adv. Mater. 34 (13) (2022) 2109920.

[25] R. Yazdian-Robati, P. Bayat, F. Oroojalian, M. Zargari, M. Ramezani, S.M. Taghdisi, K. Abnous, Therapeutic applications of as1411 aptamer, an update review, Int. J. Biol. Macromol. 155 (2020) 1420–1431.

[26] J.H. Zhou, J. Rossi, Aptamers as targeted therapeutics: current potential and challenges (vol 16, pg 181, 2017), Nat. Rev. Drug Discov. 16 (6) (2017), 440-440.

[27] X.L. Liu, F. Li, Z.L. Dong, C. Gu, D.S. Mao, J.Q. Chen, L. Luo, Y.T. Huang, J. Xiao, Z. C. Li, Z. Liu, Y. Yang, Metal-polydna nanoparticles reconstruct osteoporotic microenvironment for enhanced osteoporosis treatment, Sci. Adv. 9 (31) (2023) eadf3329.

[28] Y. Chen, Z.Q. Xu, X. Wang, X.X. Sun, X.H. Xu, X. Li, G.H. Cheng, Highly efficient photodynamic hydrogel with aie-active photosensitizers toward methicillin-resistant staphylococcus aureus ultrafast imaging and killing, ACS Biomater. Sci. Eng. 10 (5) (2024) 3401–3411.

[29] B. Li, Z. Gu, N. Kurniawan, W.Y. Chen, Z.P. Xu, Manganese-based layered double hydroxide nanoparticles as a t1-mri contrast agent with ultrasensitive ph response and high relaxivity, Adv. Mater. 29 (29) (2017) 1700373.

[30] H. Zhao, J. Lv, F. Li, Z. Zhang, C. Zhang, Z. Gu, D. Yang, Enzymatical biomineralization of DNA nanoflowers mediated by manganese ions for tumor site activated magnetic resonance imaging, Biomaterials 268 (2021) 120591.